Thermodynamic and applicability analysis of a hybrid CAES system using abandoned coal mine in China

Article · May 2018

DOI: 10.1016/j.energy.2018.05.107

Energy 157 (2018) 31–44

Contents lists available at ScienceDirect

Energy

journal homepage: www.elsevier.com/locate/energy

Thermodynamic and applicability analysis of a hybrid CAES system using abandoned coal mine in China

Jinyang Fan [a, b], Wei Liu [a, *], Deyi Jiang [a], Junchao Chen [a, b], William Ngaha Tiedeu [a], Jie Chen [a], Deaman JJK [c]

[a] State Key Laboratory of the Coal Mine Disaster Dynamics and Control, Chongqing University, Chongqing 400044 China
[b] College of Resources and Environmental Sciences, Chongqing University, Chongqing 400044 China
[c] Mackay School of Earth Sciences and Engineering, University of Nevada, Reno, NV, USA

ARTICLE INFO

Article history:
Received 12 January 2018
Received in revised form
17 April 2018
Accepted 16 May 2018
Available online 17 May 2018

Keywords:
WS-CAES
Mine roadway
Thermodynamic
Permeability
Lined cavern

ABSTRACT

China's wind and solar (WS) energy grow rapidly but simultaneously cause high wind and solar resource abandonments. Large-scale energy storage facilities, such as compressed air energy storage plants (CAES) must be complimented to balance the intermittent of these powers. However, in China's wind-solar-rich places (Three North Region), there is no salt formations for CAES construction. Thus we propose a hybrid WS-CAES system using roadways of abandoned coal mines as compressed air storage space. And the thermodynamic performance of the WS-CAES system and the suitability of roadways as compressed air storages are analyzed. This system has an average system efficiency of 50.31% and an energy storage density of 3.23 kW h/m^3. Service potential analyses of roadway were conducted for various roadway depths and different permeabilities of concrete lining and surrounding rock. It shows that roadway depth has little influence on the efficiency and output power. When the surrounding rock has a constant permeability (10^{-16} m^2), the maximum allowable permeability of concrete lining was 4.17×10^{-18} m^2. The surrounding rock with a permeability of 10^{-16}–10^{-19} m^2 could impose a significant effect on the leakage and efficiency. Finally it is indicated the main ventilation roadway and main haulage roadway have the suitability potential.

1. Introduction

The extensive utilizations of fossil fuel lead to massive greenhouse gas emission (GHGE) and environmental pollution, contributing to climate change. In addition, they will use out in the future. Renewable energy resources, such as wind power and solar power, have frequently been presented as sustainable and environmental friendly forms of energies and are expected to be a promising way to address environmental issues, reduce GHGE and satisfy future energy demand [1–4]. Therefore, massive attentions have been paid to the development of the wind and solar powers [5–9].

China has abundant wind energy and solar energy resources. The terrestrial wind power resources of 10 m above the ground level in the total reserve is approximately 3.2 TW, of which the exploitable capacity is more than 253 GW. The technological capacity of wind power resource of 80 m above the ground level is 9.1 TW with a wind speed of 6.5 m/s. The installed wind power capacity of 2016 only accounts for under 4% of total exploitable capacity (5.5 TW) [10]. The theoretical annual wind power density is greater than 200 W/m^2 in Three North Region (northeast China, northwest China and the northern areas of North China, with a total area of approx. 6,280,000 km^2). In these areas, like Qinghai province, the level of solar radiation is very considerable due to the high altitude and cloudless-ness, with an annual mean value of 8750 MJ/m^2.

In past few years China's wind and solar industry experienced a tremendous growth (Fig. 1). Since 2010, China has overtaken the United States as the largest market for wind electricity, and owns the largest absolute installed capacity for wind power, but the utilization efficiencies of wind and solar power still remain low, and the abandoned wind and solar rates remain severely high. The abandoning of wind power began from 2008 with a large new installed capacity starting to work. As shown in Fig. 2, the total abandoned wind electricity reached up to 49.7 GW h, representing up to 17% of the wind electricity in 2017. The situation of

* Corresponding author.
E-mail address: whrsmliuwei@126.com (W. Liu).

https://doi.org/10.1016/j.energy.2018.05.107
0360-5442/

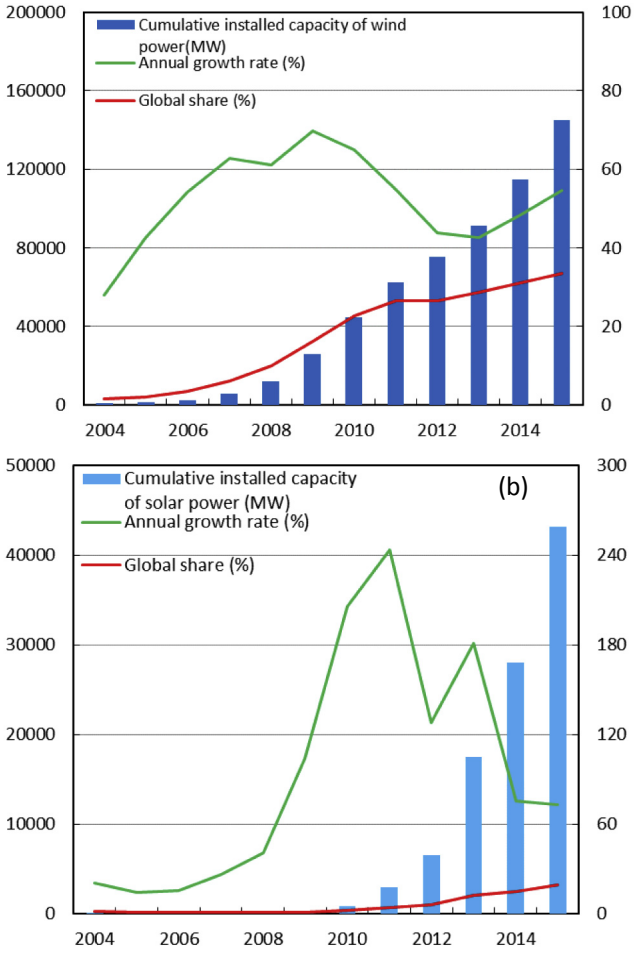

Fig. 1. Cumulative installed capacity of wind (a) and solar (b) power and their global share in 2004–2015 (Data from National Energy Administration).

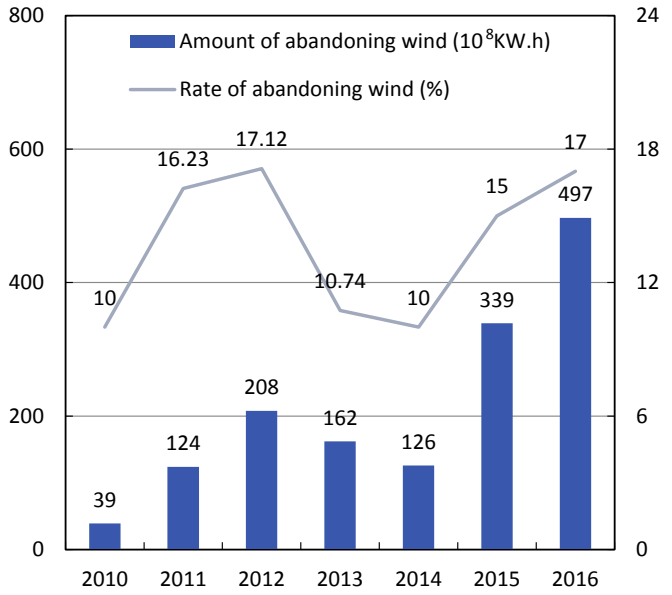

Fig. 2. Amount of abandoned wind power and the rate of abandoned wind electrical power to the total generated wind electricity in 2010–2016 (Data from National Energy Administration).

abandoning solar power is similarly serious. The rate of abandoning solar reached 22% with the quantity of 7.1 GW h in 2016 for the Three North Region.

Therefore, energy storage system (ESS) as an important link in energy supply chain is attracting tremendous attention from the Chinese government, which aims at improving the utilization efficiency of renewable energy resources and developing smart grid power networks [11–13]. A number of existing ESS technologies are economical over various time scales, but only two technologies-CAES (Compressed Air Energy Storage) and PHS (Pumped Hydroelectric Storage) are cost-effective at large temporal scales, from several hours to days [14,15]. PHS is known to require huge capital expenditures and harsh geographic conditions [16–18]. On the other hand, PHS has unknown problems of ecological pollution, potential geological disaster and people relocation. CAES could perfectly avoid such problems, thus is an ideal choice for ESS in China.

In general, the installation of CAES requires favorable geology and a suitable location [19–21]. Salt rock caverns are frequently discussed as a favorable choice for underground compressed air storage. For example, the first and second commercial CAES facilities, Huntorf CAES plant (1978) and McIntosh CAES plant (1991), both utilized underground salt caverns to store compressed air. However, up to now in China's Three North Region, no any applicable salt rock formation has been discovered.

A large number of underground caverns with huge space and good stability were formed during the exploitation of coal and then abandoned due to the problem of service life of coal mines or government policy adjustment, some of which have great potential to serve as compressed air storages. The underground space of abandoned mines does not only avoid the need for new excavation, but some surface industrial structures (buildings and living facilities) can also accommodate the equipment and staff. Therefore, utilizing abandoned mines for compressed air storage (Fig. 3) could promote the development of clean energy and simultaneously save massive investments and time. So far, the cumulative number of abandoned or closed coal mines exceeds 12,000 in China. In 2016, 2000 coal mines were shut down. An additional 1000 inefficient coal mines will be closed in 2017 [22].

A number of studies on rock caverns created by excavating hard rock formations have been performed in terms of the feasibility of its application for CAES. In the 1990s, two Japanese pilot tests of CAES were conducted in an abandoned mine [23,24]. In the United States, an abandoned limestone mine was planned to be converted into a CAES with a capacity of 2700 MW. The essential issues regarding CAES storage in underground rock caverns are the stability of the structure and permeability of sealing layer. Jonny Rutqvist and Hyung-Mok Kim [23,24] studied the geomechanical performance of a lined cavern used as CAES. As a result of the air pressure exerted on the concrete lining, tensile effective stresses could possibly cause tensile cracks, whereas effect of thermal stresses were relatively ignorable. Johansson and Mansson [25] studied the natural gas tightness in fractured granite caverns which are 50 m and 115 m underground. Synthetic linings (ordinary concrete, reinforced concrete and steel) were constructed in fractured granite and could ensure complete impermeability. However, steel lining will greatly increase the costs and rust easily in moist ambient conditions. More economical lining types (concrete lining or composite lining) needs to be investigated.

Above research demonstrated the feasibility of CAES using underground caverns. In this paper, we propose the concept of a CAES system using abandoned coal mines, coupled with wind power and solar power (WS-CAES). This WS-CAES system would convert the

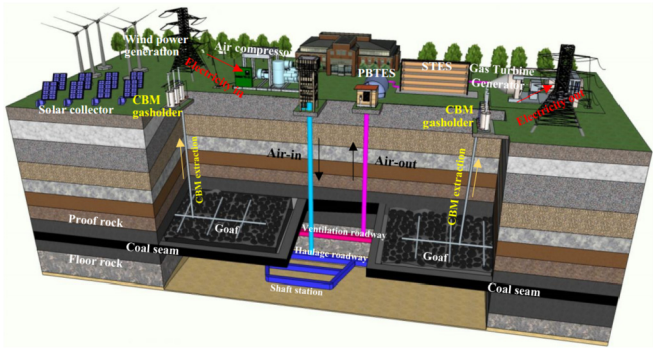

Fig. 3. WS-CAES system using mine roadways.

surplus wind electricity and solar power in China's Three North Region into compressed air energy with compressor chain and thermal energy with solar thermal collector. Solar thermal energy storage (STES) can transfer sunlight into heat and store it during daytime. During the discharging period, the compressed air flow can pass STES and increase the system output [16,26,27], thus is adopted. Based on the typical geological condition and meteorological data of Three North Region in China, the suitability potential of coal mines in terms of the roadway depth, permeability of concrete and surrounding rock, was investigated. The different types of mine roadways serving as compressed air storages were analyzed, and the feasibility of using abandoned coal mines as WS-CAES was discussed at the national energy strategic level.

2. System description

Considering the shortage of water and an ambient temperature below 0 °C in winter in the Three North Region, the heat exchangers use a solid medium, a packed bed of natural rocks thermal energy storage (PBTES), which has the advantages of low cost, high efficiency and reliability [28]. The system schematic diagram is shown in Fig. 4, consisting of two processes: the charging process and discharging process. In the charging process, air is compressed three times by three compressors (the sequence from left is CP1, CP2, and CP3). After each compressor, a PBTES (the sequence from left is PBTES1, PBTES2, and PBTES3) is installed to cool the outlet air to ambient temperature and then store the thermal energy. The highly compressed air leaving the last PBTES will enter lined mine roadways (LMR). During the discharging process, energy is retrieved by withdrawing air under a high pressure. Before entering turbines (the sequence from left is T1, T2, and T3), the compressed air passing through PBTESs is preheated and then heated again by STESs (the sequence from left is STES1, STES2, and STES3). PBTESs will naturally cool down to ambient temperature after every discharging process ends. To maintain a constant expansion ratio for the entire discharge process, a throttling valve system is set at the outlet of LMR. A constant-pressure air is provided for turbines to generate electricity.

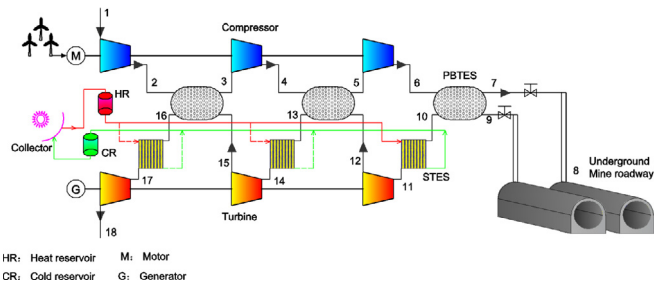

Fig. 4. Schematic diagram of the WS-CAES power plant.

3. Model for the WS-CAES system

The following assumptions are made to simplify the analysis of the system:

(1) The air in CAES systems consists of 77% N_2 and 23% O_2 (mass fraction).
(2) The system works at steady state conditions;
(3) The compressors and turbines have fixed isentropic efficiencies;
(4) All kinetic and potential effects are ignored.

3.1. Compressors

Based on the fixed pressure ratio, the outlet pressure of the compressor can be expressed as follows:

$$P_{c,out} = \pi P_{c,in} \tag{1}$$

Inlet pressure $P_{c,in}$ should be equal to the ambient pressure P_0 for CP1. The outlet temperature T can be determined by

$$T_{c,out} = T_{c,in}\left[1 + \left(\pi^{\frac{\gamma_0-1}{\gamma_0}} - 1\right)\Big/\eta_c\right] \tag{2}$$

where γ_0 is the ratio of specific heats, η_c is the isentropic efficiency of the compressors. When the unit mass of air passed the compressor, the compressor work w_c of unit mass of air is

$$w_c = c_{p,a}(T_{c,out} - T_{c,in}) \tag{3}$$

where $c_{p,a}$ is the heat capacity of air. The exergy destruction $\dot{e}$ associated with a compression is calculated by

$$\dot{e}_c = c_{p,a}\left[(T_{c,out} - T_{c,in}) - T_0 ln\frac{T_{c,out}}{T_{c,in}}\right] + T_0 R_g ln\pi \tag{4}$$

3.2. Turbines

Turbines were modelled through mass and energy balance following the same approach adopted for the compressors.

$$P_{t,out} = P_{t,in}/\beta \tag{5}$$

$$T_{t,out} = T_{t,in}\left[1 - \left(1 - \beta^{\frac{\gamma_0-1}{\gamma_0}}\right)\eta_t\right] \tag{6}$$

where β is the expansion ratio. The output work per unit mass and the total work of each turbine are

$$w_t = c_{p,a}(T_{t,in} - T_{t,out}) \tag{7}$$

3.3. PBTES

According to the results presented in Ref. [29], cooling/preheating effect of PBTESs is initially unsteady and will become steady after several cycles (~20 cycles) of absorbing/releasing heat.

In the 1st cycle, the outlet temperature could remain constant, equal to ambient temperature. After 20 cycles, PBTES could remain the outlet temperature at ambient temperature in the initial 70% charging period, while in the remaining 30% period the cooling effect get worse. The outlet temperature rises approximately 100 K. During the first several cycles, PBTESs are only able to preheat the air to a constant value in the initial 70% period, then the outlet temperature decreases approximately 100 K. The preheating effect could remain constant after 20 cycles. To simplify the analysis, the outlet temperature of air during charging and discharging is assumed to be constant as in the first initial 70% stage. The pressure drop across the PBTES system is estimated by Ergun's equation.

$$\frac{\Delta P}{L}=\frac{150\mu u_a}{d_p^2}\left(\frac{1-f}{f}\right)^2+1.75(1-f)f\frac{\rho_a u_a^2}{d_p^2} \tag{8}$$

where u_a is the average velocity of the air. The heat loss of PBTES through the wall is approximately evaluated by calculating the thermal resistance of insulating cylindrical layer.

$$\Delta\dot{T}=\frac{T_{inner}-T_0}{R_{th}m_s c_s} \tag{9}$$

where T_{inner} is the average temperature of a packed bed rock. According to Fourier's law of heat conduction, the thermal resistance is given by:

$$R_{th}=\frac{\ln\left(\frac{r_{wa,ex}}{r_{wa,\ in}}\right)}{2\pi Lk_w} \tag{10}$$

Where $r_{wa,\ in}$ and $r_{wa,ex}$ represent the inner and external radius of PBTESs, respectively. The exergy destruction $\dot{e}_{xi}$ can be calculated by

$$\dot{e}_{xi}=c_{p,a}\left[(T_{xi,out}-T_{xi,in})-T_0 ln\frac{T_{xi,out}}{T_{xi,in}}\right]+T_0R_g ln\frac{P_{xi,out}}{P_{xi,in}} \tag{11}$$

3.4. STES

Clean solar resource in North China is adequate. Solar collector could transfer the solar power into thermal resource, which can be stored and used to pre-heat compressed air during discharging. The collected heat can be evaluated by

$$Q=\alpha A J_T\eta_{so}(1-\eta_L) \tag{12}$$

where α, η_{so}, η_L are solar fraction, efficiency of collector and heat loss rate. The outlet temperature can be obtained from heat absorption. The stress drop through STES is approximately estimated with pressure loss coefficient ε, which normally takes the value of 0.003.

$$\Delta P=\varepsilon P \tag{13}$$

3.5. Pipe

Friction between the fluid and pipe wall will cause the pressure loss, which can be evaluated by

$$\frac{\Delta P}{L}=\frac{\lambda}{d}\frac{\rho_a u_a^2}{2} \tag{14}$$

Where λ is drag efficiency and can be calculated with absolute friction.

$$\lambda=0.11\left(\frac{K}{d}\right)^{0.25} \tag{15}$$

K is the absolute roughness of pipes. d is the diameter of the pipe and ρ_a represents the air density.

3.6. Throttling

The throttling valve is to give a constant working pressure for turbines. The flow inside is isenthalpic and the exergy destruction can be expressed by:

$$\dot{e}_{tv}=T_0R_g ln\frac{P_{tv,out}}{P_{tv,in}} \tag{16}$$

3.7. Compressed air storage

It is assumed that leaking air flow through lining and surrounding rock is slow and observes Darcy's law. The air flow velocity v is determined by

$$v=\frac{k}{\mu}\frac{dP}{dr} \tag{17}$$

where r is the distance to center of lining, k is the permeability of surrounding rock or concrete lining, P is air pore pressure. Using Finite Element Method, the seepage velocity of air through the concrete lining surface can be obtained.

$$\dot{m}=\oint v\rho_a dA_{lin} \tag{18}$$

Mass leakage rate can be calculated by integration.

4. Thermodynamic performance

In this section, the air storage is considered completely tight, that is, the leakage rate is zero.

4.1. Performance indicator

The total efficiency of the system η_{sys} is defined as

$$\eta_{sys}=\frac{\sum w_t}{\sum w_c+\sum Q} \tag{19}$$

Indicators *SE* and *WE*, which indicate the efficiency of solar heat and wind power converted into electricity, respectively, are defined as

$$SE=\frac{\sum w_t-\sum w_t(J_T=0)}{\sum Q} \tag{20}$$

$$WE=\frac{\sum w_t(J_T=0)}{\sum w_c} \tag{21}$$

where $\sum w_t(J_T=0)$ indicates the outputs of the system when $J_T=0$. Indicator *SIR* and *SOR* represent the share of the input and the final output energy contributed by the solar power, respectively.

$$SIR = \frac{\sum Q}{\sum w_c + \sum Q} \tag{22}$$

$$SOR = \frac{\sum w_t - \sum w_t(J_T = 0)}{\sum w_t} \tag{23}$$

EPV, an index of energy generated per unit volume of the cavern, is employed to assess the energy storage density, which is:

$$EPV = \frac{\sum w_t T_{dc}}{V_{cav}} \tag{24}$$

4.2. Typical Cycle Analysis

4.2.1. Design parameters

The operation mode has a charging period of 8 h and a discharging period of 4 h (Fig. 5), typical for existing CAES plants [16,30]. The storage pressure is set at 7.5 MPa and the minimum working pressure is 4.0 MPa. The underground space of the storage reservoir is 24762 m^3 (which is obtained with the working pressure and air flow 20 kg/s). Maximum daily solar irradiation and ambient temperature are 22 MJ/m^2 and 279.55 K, respectively, according to the data from China Meteorological Administration for Xinjiang province. Maximum solar heat storage rate, which indicates the ratio of stored heat in STESs to compression work, is set at 0.855. Solar trough system would be employed for energy collection; Dowtherm A (a eutectic mixture with 73.5% diphenyl ether and 26.5% biphenyl) was used as the heat transfer medium because of the relatively large temperature range of its liquid state. The temperature of Dowtherm A after heated by solar collector is assumed at 650 K and reduces to 563–549 K at exits of STESs. Other design parameters and detailed conditions for the simulation and analysis of the compressed air energy storage are summarized in Table 1.

4.2.2. Parametric analysis

Parametric analyses were conducted with one parameter varying and some affiliated parameters (such as, air temperature, compression work, expansion work, system output work and EPV) varying correspondingly, whereas others stay constant.

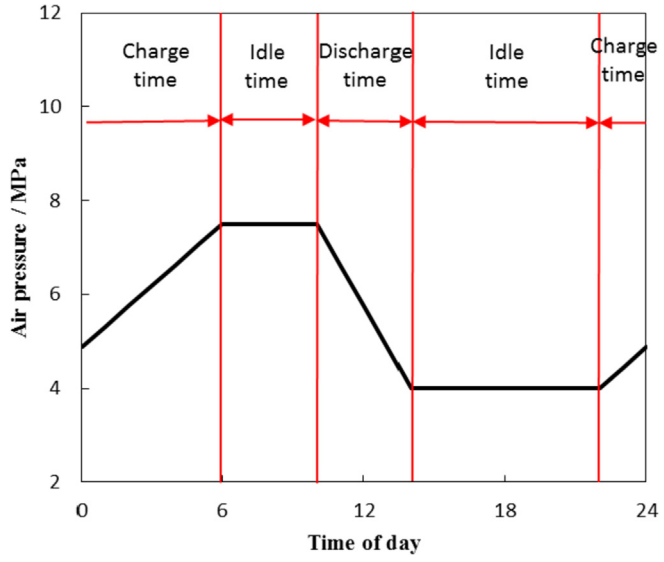

Fig. 5. Operation mode of the WS-CAES.

a) Varying minimum working pressure

To provide a constant pressure ratio for turbines, the working pressure will be adjusted to a constant value (normally minimum working pressure) before entering turbines. According to Eq. (16), the exergy loss can be reduced by increasing the outlet gas pressure, thus changing the system performance. The system output power, EPV and system efficiency were calculated (see Fig. 6). In terms of the underground space utilization, the outlet gas pressure is better to be at 4 MPa where the storage cavern has the maximum power generation, 8.09 MW, and the maximum EPV, 2.99 kW h/m^3 (hollow points in Fig. 6). It is therefore that the minimum working pressure is set at 4.0 MPa.

b) Varying air mass flow

Large air mass flow would increase the pressure loss as the air flow passes through the system components, especially the PBTESs. Fig. 7 shows the relationship of exergy loss, pressure drop and mass flow of air through the first PBTES. It can be seen that exergy loss and pressure drop increase significantly with air mass flow. As the air flows through PBTES1, PBTES2 and PBTES3, the pressure exergy loss decreases rapidly, because the increasing density of air after compression reduces the air flow velocity and thus diminishes the friction when air flows through PBTESs.

c) Varying solar heat storage rate

PBTESs employed in the system can improve the system performance (Fig. 8) in terms of output power and system efficiency. This improvement depends on the amount of heat stored in and recovered from the PBTESs. Fig. 9 shows the temperature difference between node 12 and node 13 over various solar heat storage rates (which measures the amount of heat recovered from PBTES2) with different ambient temperatures. As the solar heat storage rate increases, the temperature difference decreases. When the temperature difference becomes zero, the rate is around 0.855. To ensure that the system could reuse the heat stored in PBTESs, the stored heat should be less than this value. It can be seen that the maximum solar heat storage rate is almost the same at different ambient temperatures (253 K–313 K). Consequently, the solar heat storage rate is set at 0.855 (Table 1).

4.2.3. Exergy analysis of a typical cycle

The temperature and pressure at each node of the CAES system are given in Table 2. The exergy change and exergy loss of the air through each system components (shown in Table 3) were calculated with Eqs. (4), (11) and (16). It can be seen that there are two exergy sources: compressors generate 75.7% of the total exergy while STESs provide the remaining 24.2%. Compressors convert the electricity into the mechanical exergy and thermal exergy of air, having an exergy efficiency of 89.9%. STESs have a relatively low exergy efficiency, only 43.8%, which will reduce the whole CAES system efficiency. Although the STES can raise the power output of system, it is unreasonable to install STESs without limits. The maximum solar heat rate has been discussed previously. PBTESs do not generate any exergy, but temporarily store the thermal energy of air after compression and use it to preheat the air before expansion, reducing the work of compressors on one hand, simultaneously providing thermal exergy to the system like STESs on the other hand. It can be understood that compressors only provide pressure exergy (57.6%), while the thermal exergy is supplied by STESs (24.2%) and PBTESs (18.2%). Fig. 10a shows the share of generated exergy.

In the exergy consumption side, most of the exergy (74.0%) is

Table 1
Basic parameters used in the thermodynamic model.

Charging time (hour)	8	Isentropic efficiency of compressors and turbines	0.88
Discharging time (hour)	4	Pressure ratio	4.20
Ambient temperature (K)	279.55	Expansion ratio	3.39
Atmospheric pressure (Pa)	101325	Air flow (Kg/s)	20
Burden Depth (m)	10	Maximum daily solar irradiation (MJ/m^2/day)	22
Roughness of pipe (m)	0.0002	Diameter of pipe (m)	0.5
Cavern space (m^3)	24762	Solar heat storage rate	0.855
Porosity	0.36	Length of PBTES (m)	5
Diameter of solid particles (m)	0.03	Radius of PBTES (m)	2
Thickness of insulating wall (m)	0.1	Heat conductivity of wall (W/(m*K))	0.0036
Pressure loss efficiency of STES	0.003		

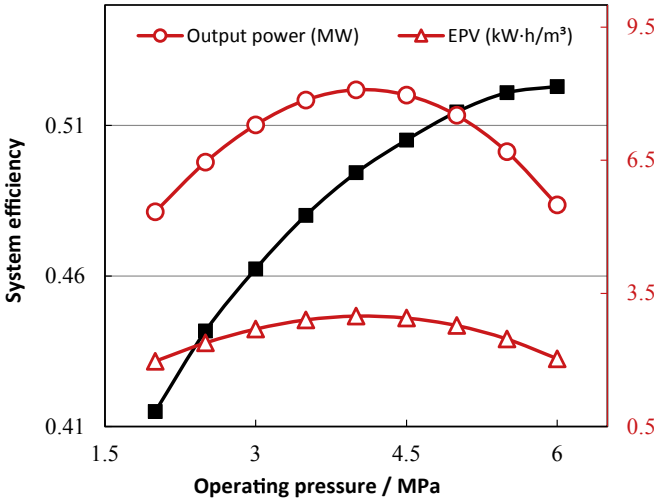

Fig. 6. System efficiency and output power of the WS-CAES system.

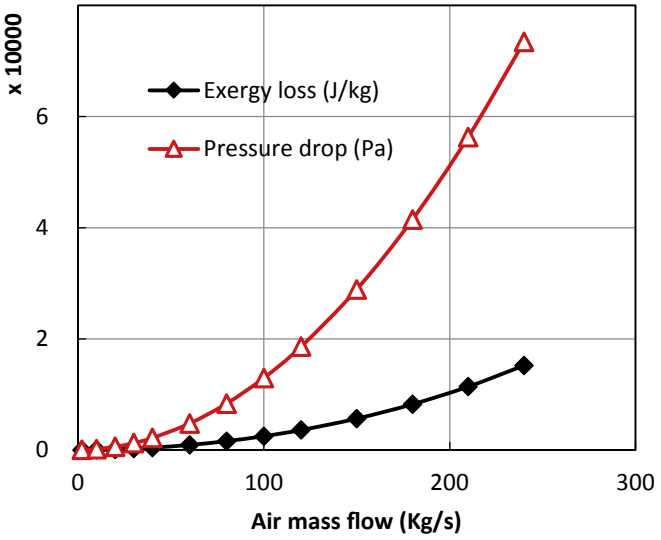

Fig. 7. Exergy loss and pressure drop caused by compressed air passing through the first PBTES.

used to generate electricity with an exergy efficiency of 90.5%. 26.0% exergy was lost due to the heat loss of heat exchangers (PBTES), pressure regulation of throttling valve, the gas friction during the air through the system components, etc.

For a perfect design of CAES system, the exhaust temperature should be close to the ambient temperature after the last expansion. From Table 2, it is obvious that the exhaust temperature is approximately 130 K over the ambient temperature, and thus a certain amount of waste heat in exhaust air remains, accounting for 3.8% of the exergy. To make full use of the waste heat, ORC system using R123 turbine can be employed to decrease the outlet temperature of exhaust air by 80 K [31]. More details on the ORC system are given in Ref. [15]. But it is noteworthy that the ORC subsystem has a low converting efficiency which can only raise the system efficiency by 0.8% if the design conditions in Ref. [31] are applied.

The pressure exergy loss of air through the throttling valve during charging and discharging period takes up to 6.0% of exergy consumption (Fig. 10b). Heat loss of PBTESs only amounts to 0.2% of the total exergy consumption. The exergy loss caused by pipe friction is so small that it is usually neglected in many publications [28,31–33].

4.3. A case study for WS-CAES in Xinjiang province

The temperature periodically changes in accordance with four seasons. The maximum annual temperature difference could reach 60 K in North China. The biggest average monthly temperature difference is about 40 °C. As shown in Fig. 11, the system efficiency (including *SE* and *WE*) is independent of the ambient temperature, but the output power and stored energy density (EPV) increases almost linearly with ambient temperature.

Xinjiang province, the richest area for wind and solar resources in China, is taken as the example, where the lowest monthly average temperature is −12 °C in January. It gets warmer gradually till July (21 °C) and then cools through autumn and winter. Solar irradiation rate, defined as the ratio of daily solar irradiation to its maximum value, indicates the variation of solar irradiation (Fig. 12). The maximum solar irradiation of Xinjiang province is 21.87 MJ/day, appearing in June.

Based on the data shown in Fig. 12, the output of a WS-CAES plant is shown in Fig. 13. With the increase of solar irradiation, the solar input share (*SIR*) and output power (*SOR*) both go up, reaching a peak in June. But the *SOR* is always below the *SIR*, because of the low converting efficiency of the solar power. The wind output power follows a similar trend, but reaches its peak in July, since it is affected by the ambient temperature. The average system efficiency, power and EPV reach 50.31%, 8.76 MW and 3.23 kW h/m^3, respectively.

5. Suitability potential for abandoned coal mines

In this section, we analyze the effects of roadway depth, the permeability of the concrete lining permeability and surrounding rock and then discuss the service potentials of different types of roadways. The geometrical model of a coal mine roadway is shown in Fig. 14 and the values adopted for the parameters are listed in Table 4. In order to avoid the influence of mining activities,

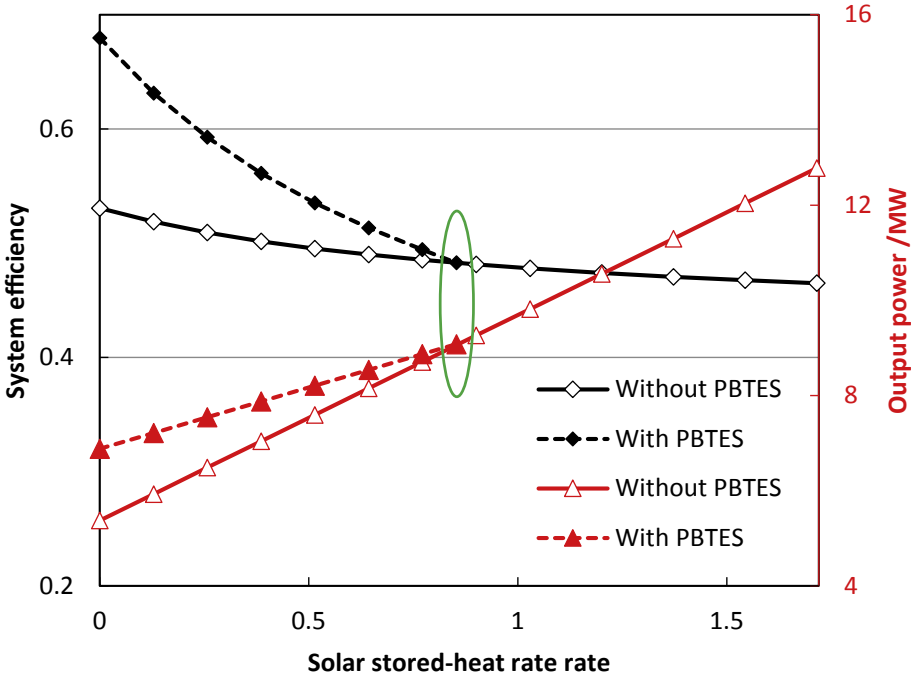

Fig. 8. System efficiency and output power with various solar stored-heat rate rates.

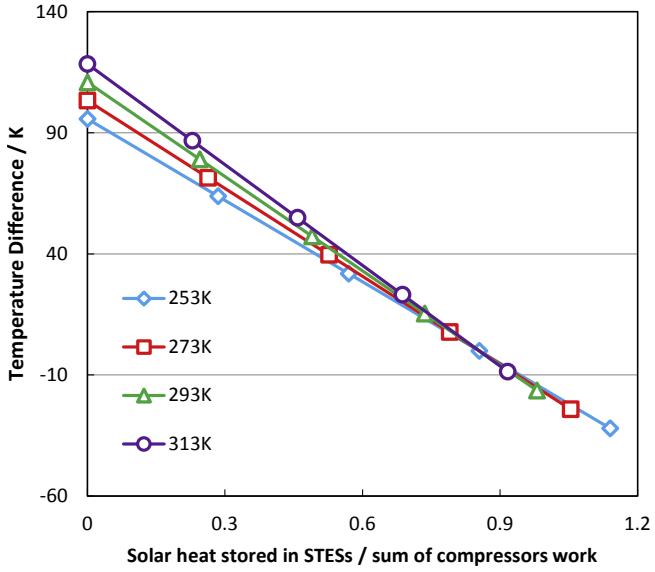

Fig. 9. Temperature difference between the node 12 and node 13 over various solar heat storage rates.

principal roadways usually are located in floor rock beds 20–30 m away from the overlying coal beds. Their surrounding rocks are relatively fixed and intact. Surrounding rock 1 represents the intact stratum which has a thickness of 10 m and a permeability of 10^{-14} m^2, common normal values for surrounding rock in coal mines. Surrounding rock 2, which has a higher permeability of 10^{-12} m^2, represents the strata influenced by mining activities.

Ref. [23] assumed the water table to be close to the ground surface, which can reflect most cases of underground caverns, whereas it is mismatching with abandoned coal mines. Usually a drainage system is employed for a coal mine to prevent floods threatening the working places. Thus, the underground water is

Table 2
Temperature and pressure at each node of the system.

Node	Temperature (K)	Pressure (Pa)
1	279.55	101325
2	441.26	425565
3	279.55	424986
4	443.29	1784944
5	279.55	1784805
6	454.22	7496182
7	279.55	7496147
8	279.55	7495997
9	279.55	4000000
10	453.33	3999909
11	562.26	3987909
12	417.60	1179914
13	442.46	1179366
14	551.38	1175828
15	411.66	346852
16	440.44	345025
17	549.37	343990
18	410.68	101472

assumed to be always zero. The air pressure inside the mine roadways can be set at the average value (5.46 MPa) under the typical operation mode shown in Fig. 5, because of the linear relationship between leakage flow and air pressure, according to Darcy's law. The annual average temperature of 6.4 °C and solar irradiation rate of 0.76 were applied in the WS-CAES system performance calculation.

5.1. Roadway depth effect

Hyung-Mok Kim's research showed that increasing the cavern depth from 100 m to 500 m could reduce the leakage rate by about two orders of magnitude. The reduction of the leakage rate was explained by the relatively reduced permeability in the lining and the reduced pressure gradient resulting from the increased hydrostatic liquid pressure with depth [23]. Here, we take the experimental results of concrete in Ref. [34] as reference which

Table 3
Exergy change and loss during processes.

System component	Quantity of heat or work (J/Kg)	Exergy Change (J/Kg)	Exergy loss(J/Kg)			Generated electricity (J/Kg)
			Mechanical	Thermal	Remaining	
CP1	163653.6	+149697.1				
CP2	165703.8	+150451.5				
CP3	176764.0	+154621.4				
STES3	110229.5	+49311.9	241.1			
STES2	110229.5	+47968.2	241.1			
STES1	110229.5	+47712.6	241.1			
PBTES3			2.2	343.8	0	
PBTES2			43.5	309.6	24140.3	
PBTES1			533.0	303.4	22234.8	
TV			34904.4			
PIPE			2.0			
T1		−160227.4	13840.2			146387.2
T2		−156707.7	15309.1			141398.6
T3		−156020.9	15672.2			140348.6
Exhaust air					21926.4	

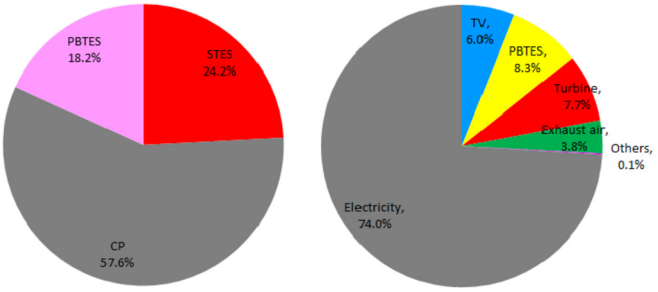

Fig. 10. Generated exergy share of each component (a); Exergy loss share of each component (b).

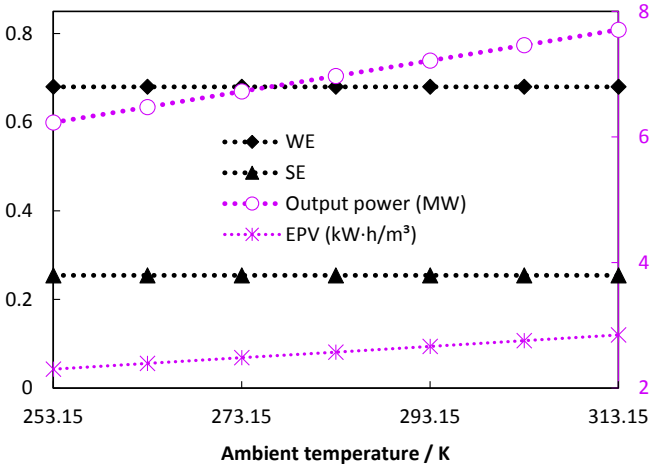

Fig. 11. System efficiency *vs* ambient temperature.

showed the permeability of the concrete lining only changed slightly (Fig. 15).

Fig. 16 shows the air pressure distribution and leakage flow direction in the vicinity of the roadway at the depth of 100 m. It can be seen that the air can also seep through the floor rock. The mass flow of air through the concrete lining can be automatically calculated by software with integration. As the mining depth goes from 100 m to 600 m, the air distribution almost remain unchanged, only the air leakage flow and leakage rate within one day (24 h) show a minor decrease (Table 5). Fig. 17 shows the annual average of system efficiency and output power of CAES for various cavern depths when the annual average temperature and solar irradiation rate are 6.4 °C and 0.76 respectively. Increasing the depth from 100 m to 600 m just raises the annual average system efficiency, output power and EPV by 0.35% and 0.058 MW, respectively. Therefore, the cavern depth has little influence on the system performance. However, necessary depth should be guaranteed to prevent tensile cracking as a result of the over air pressure exerted on concrete lining [23,24].

5.2. Effect of concrete and rock permeability

Fig. 18 shows the air pressure distribution as the concrete permeability increases from 10^{-19} m^2 to 10^{-16} m^2. It can be seen that the pressure-changing area gradually shifts from concrete lining zone to surrounding rock. When the permeability of the concrete lining is greater than 10^{-16} m^2 or lower than 10^{-19} m^2, the pressure-changing area remains fixed, implying that the air seepage of storage reservoir mainly depends on the concrete lining with the permeability above 10^{-19} m^2, as well as the surrounding rock with the concrete permeability below 10^{-16} m^2.

The leakage rate and system efficiency of the WS-CAES with are shown in Fig. 19. Above 10^{-16} m^2, the leakage rate almost remains constant at 2.4%; below 10^{-19} m^2, the leakage rate is reduced to a negligibly small value. The leakage rate of compressed air storages reservoir is suggested to be less than 1% for one day (one cycle). When the surrounding rock has a constant permeability of 10^{-14} m^2, the maximum allowable concrete lining permeability is obtained, 4.17×10^{-18} m^2.

At present, it is difficult to achieve the permeability of 4.17×10^{-18} m^2 with ordinary concrete [34–36]. Although RPC (reactive powder concrete) has favorable permeability (~10^{-20} m^2), it is characterized by high cost and excess contractibility, limiting its application in underground engineering [37,38]. Therefore, it is important to select a suitable place having an extremely low permeability to ensure the tightness of the storages. It can be understood that the concrete lining tends to keep the structure stability and surrounding and is responsible for the airtightness in function.

Fig. 20 shows the leakage rate and system efficiency of the WS-CAES with various permeabilities of the surrounding rock (Surrounding rock 1). To maintain the leakage rate below 1%, the surrounding rock should have a permeability below 10^{-15} m^2, which is feasible in coal geology. As the permeability exceeds 10^{-16} m^2, the leakage rate rises sharply. When the surrounding rock is completely

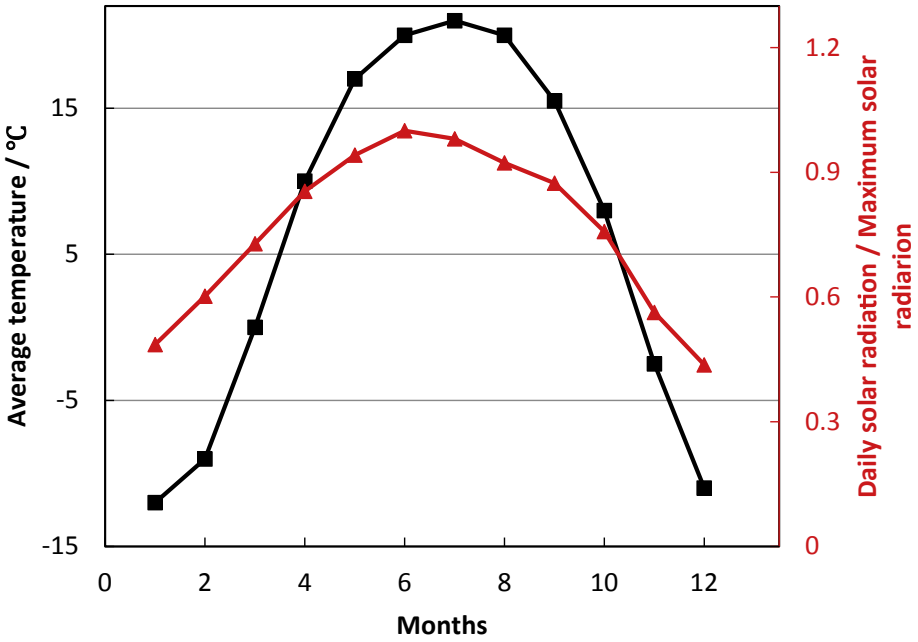

Fig. 12. Average temperature and daily solar irradiation in 12 months (Data from China Meteorological Administration).

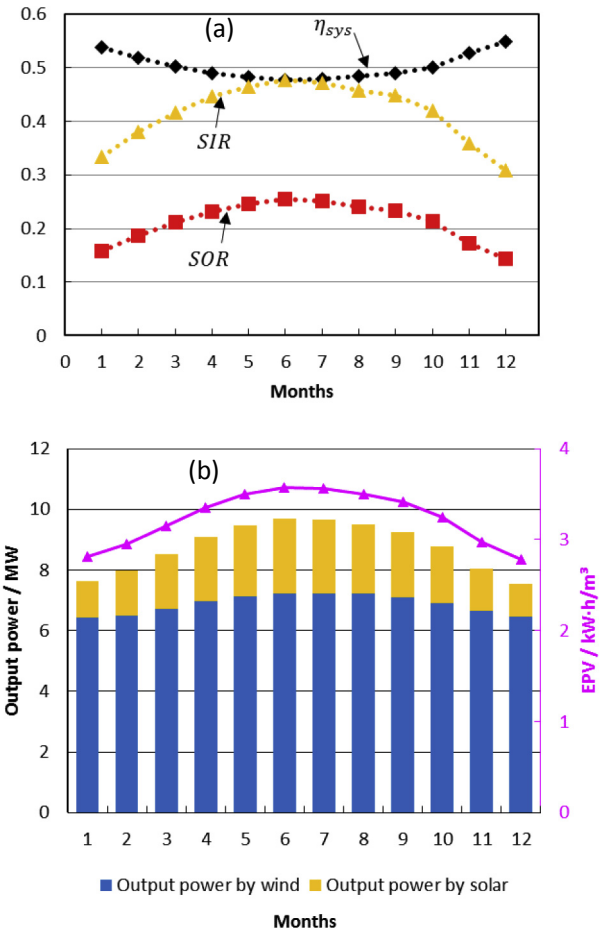

Fig. 13. System efficiency, *SIR* and *SOR* (in Figure a), Output power and EPV (in Figure b) of a CAES based on the data of Xinjiang Province.

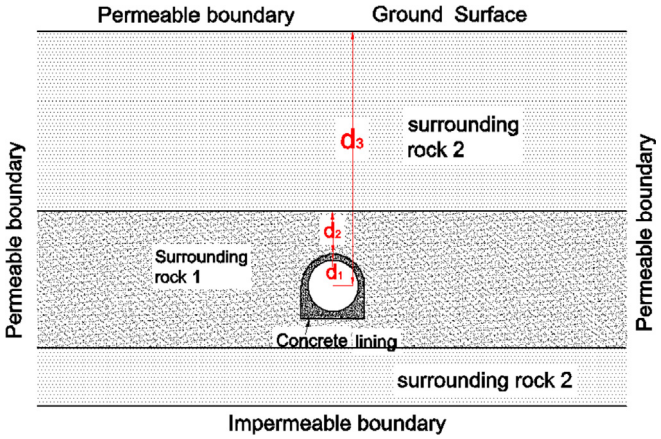

Fig. 14. Geometrical model of a coal mine roadway.

influenced by mining activities, the leakage rate within one day would come to a huge value, 36.7%.

5.3. Different types of roadway

Airtight surrounding rock is critical to the underground compressed air storage. Various types of caverns are formed during mine construction and coal excavation. There are mainly three types of roadways in terms of service scope and service life: development roadway, preparation roadway and mining roadway. Preparation roadway and mining road (including coal bunker etc.) often serve for one or several mining areas for two or three years. They are arranged in coal beds, where the surrounding rock is largely damage fragmented after coal is extracted, and therefore they have little chance to provide an airtight condition. Development roadway is usually constructed in solid rock beds and serves the whole mine for the whole life (usually 30–80 years), having the potential to be used as the storage caverns of compressed air. Development roadway mainly includes shafts, main ventilation

Table 4
Adopted values of parameters for the model in Fig. 14.

Inner radius of the roadway (m)	1.5	Initial permeability of Concrete k_{cc} (m^2)	10^{-16}
d_1 (m)	0.3	Initial permeability of surrounding rock 1 k_{sr1} (m^2)	10^{-14}
d_2 (m)	5	Permeability of surrounding rock 2 k_{sr2} (m^2)	10^{-12}
d_3 (m)	26.8	Thickness of surrounding rock 1 (m)	10
Width of the model (m)	50	Thickness of surrounding rock 2a, 2b (m)	20, 5

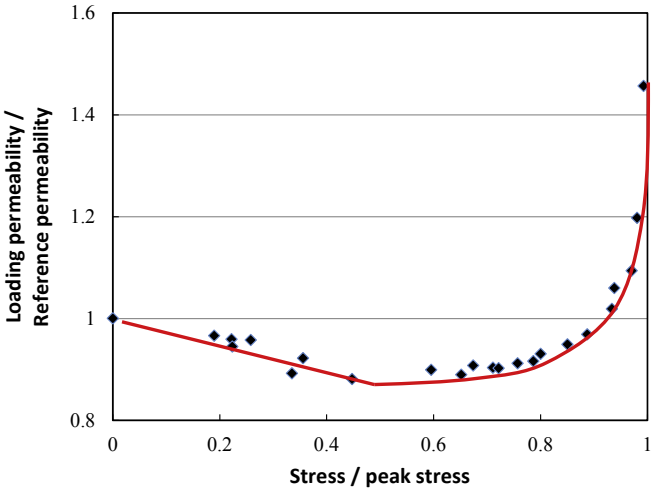

Fig. 15. Permeability of ordinary concrete [34].

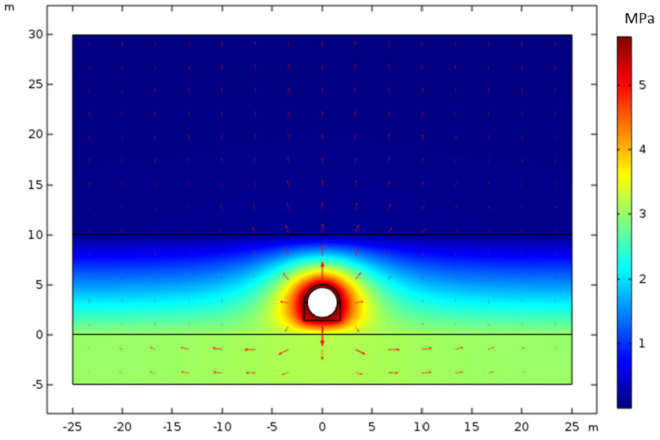

Fig. 16. Air pressure distribution and air flow direction at 100 m depth.

roadway and main haulage way.

Mine shaft is the channel to connect surface and underground workplace. It passes through epipedon, aquifer, coal seam etc. Shafts located at different depths may have different permeabilities. It is difficult to ensure that every stratum has suitable permeability. On the other hand, if the air pressure is exerted on the shaft wall, the upper shaft wall in shallow depth could easily crack. Therefore, a mine shaft is also unfit to serve as compressed air storage. Since underground has a relatively better heat preservation effect, mine shaft can be deposited the solid particles of PBTES or the media (high temperature thermal oil) of STES to save some amount of excavation work.

Main ventilation and haulage roadways are always located where surrounding rocks are relatively intact, usually in the floor rock beds 20–30 m away from the overlying coal beds. From statistical data in Fig. 21, gas pressure in coal formations at the depth of 600 m can exceed 7 MPa [39], which implies that the system constituted by coal formation and its surrounding rock can have sufficient air tightness. Some kinds of common surrounding rocks (including mudstone, shale, silt sandstone, packsand, argillaceous siltstone) were collected from coal mines and their permeability was tested [40–42]. Their leakage rates and corresponding system efficiencies are given in Fig. 20, showing that mudstone can provide a considerable air tightness. Therefore, the surrounding rock of main ventilation/haulage roadway below 600 m is able to have a considerable air tightness, having a good potential for compressed air storages.

6. Discussion and prospect

According to above analyses, a typical abandoned coal mine with 3.5 km long usable roadway could be constructed as a WS-CAES plant with an 8.76 MW output. In 2016, China's installed wind and solar power capacity reached 1.7×10^5 MW and 0.2×10^5 MW, respectively. From the government's mandatory suggestion, the energy storage facility should match at least 10% of installed wind power capacity [43]. If all the energy storages are realized by WS-CAES plants, at least 6800 km long usable roadway of abandoned coal mine is required, equivalent to 1944 coal mines. The data from China Coal Industry Association shows that there are approximately 15,000 abandoned coal mines at present, 17% of which (2550) belong to highly gassy mines that have a considerable airtight surrounding rock system. Therefore, developing WS-CAES plant using abandoned coal mines is feasible in the short term.

According to national medium-long-term plan, China's installed wind power capacity will go up to 5.0×10^5 MW in 2030, 10×10^5 MW in 2050 [44]. The solar power is predicted to have an installed capacity of 1.0×10^5 MW in 2020, 4.0×10^5 MW in 2030, and 10×10^5 MW in 2050, respectively [45,46]. The required roadways of abandoned coal mine cannot be less than 35,960 km,

Table 5
Mass flow of air through concrete lining with unit length and the corresponding leakage rates.

Mining depth/m	Mass flow of air through cavern reservoir with unit length/Kg(d·m)$^{-1}$	Leakage rate/%
100	1221.09	2.3289
200	1219.97	2.3268
300	1218.84	2.3247
400	1217.72	2.3225
500	1216.60	2.3204
600	1215.48	2.3182

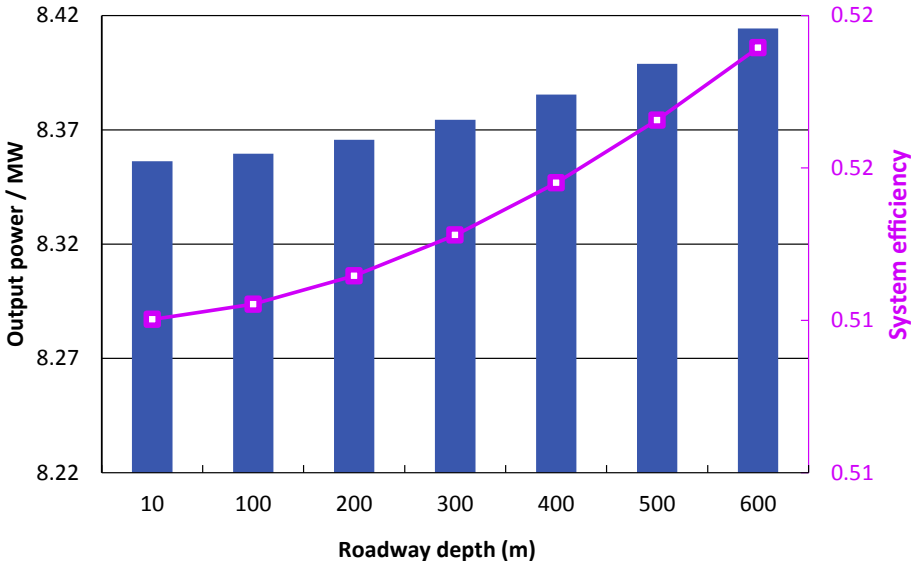

Fig. 17. Average system efficiency and output power of CAES under various cavern depth.

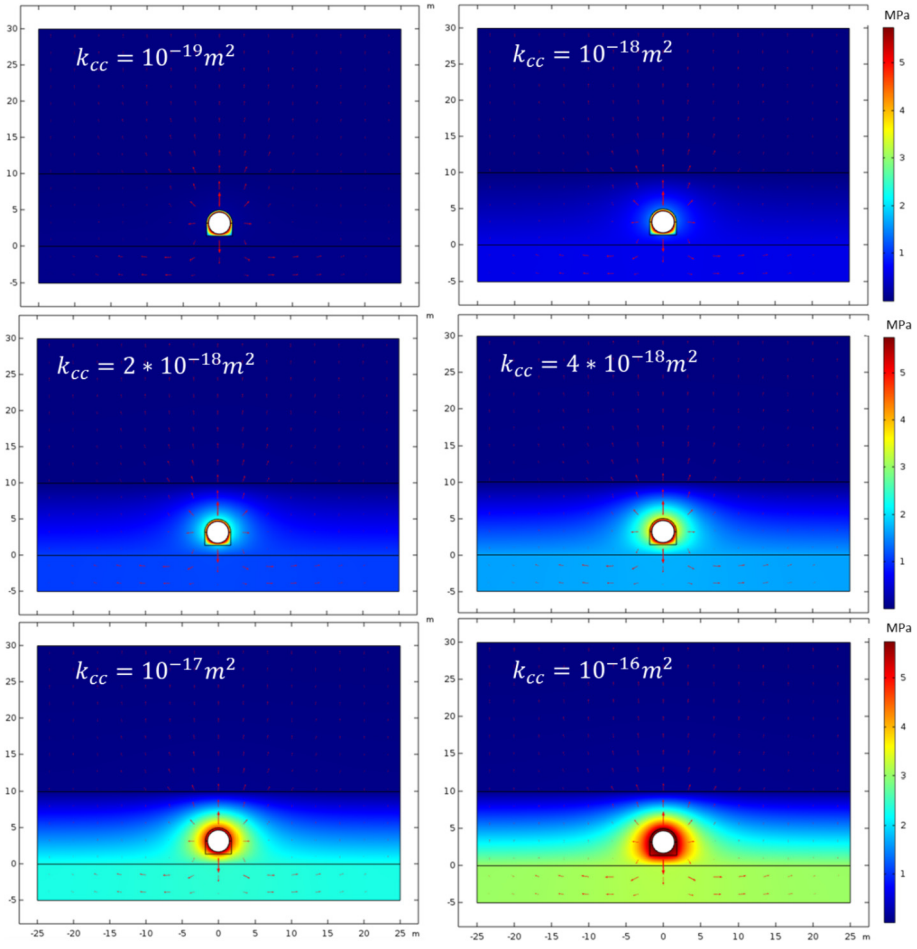

Fig. 18. Air pressure distribution as the permeability of concrete lining (κ_{cc}) increases from 10^{-19} m^2 to 10^{-16} m^2.

equivalent to 10,273 coal mines, by 2030. The present number of abandoned coal mines is still enough for the medium-term plan (2030). However, the abandoned coal mines are obviously insufficient for the long-term plan of wind-solar power (2050). So it is necessary to develop higher-density energy storage technologies or improve the existing ESS.

Recently, a hot topic is becoming more and more popular: abandoned coal mines are suggested by some scholars to develop

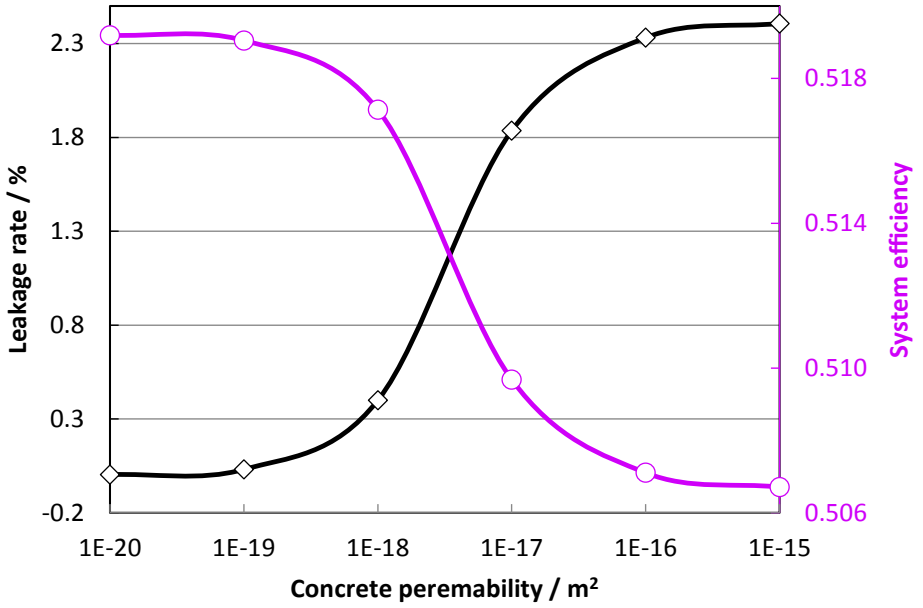

Fig. 19. Leakage rate and system efficiency of the WS-CAES as the permeability of concrete lining increases from 10^{-21} m^2 to 10^{-16} m^2.

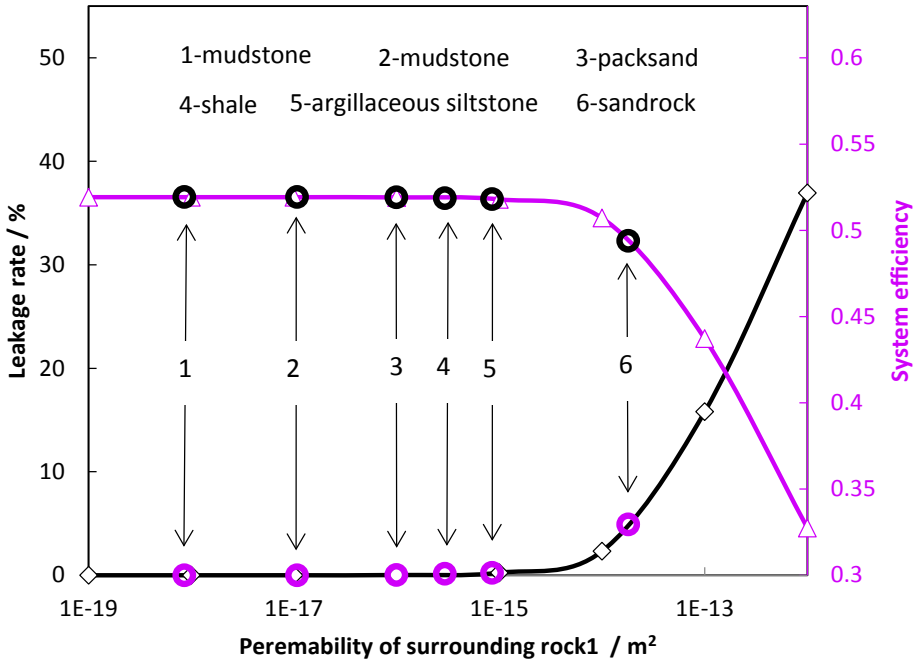

Fig. 20. Leakage rate and system efficiency of the WS-CAES as the permeability of the Surrounding rock 1 increases from 10^{-20} m^2 to 10^{-13} m^2.

PHS plants [47]. In the perspective of energy storage density, WS-CAES technology has obvious advantages. A 600 m deep coal mine used as PHS plant could only have an energy storage density of 1.67 kW h/m^3, much less than that of WS-CAES plant. In addition, in Three North Region water resources are significantly lacking to support the PHS plants. Using abandoned coal mines as WS-CAES has another two advantages making it the more promising ESS technology on the national strategic level. After coal mines are shut down, there is some residual coal in the goaf, which contains a large amount of residual coalbed methane, because of the problem of low coal recovery rate ($\sim 2/3$) in China. The drainage and utilization of coalbed methane has been attracting massive attentions from policy makers and scholars [47]. In 2016, China has an annual coalbed methane production of 7.48 billion m^3 [48,49]. Using it as afterburning gas of the WS-CAES (Fig. 3) can get double benefits, increasing the output of CAES and saving the transport cost. Secondly, a higher energy storage density can be achieved by increasing the operational gas pressure of WS-CAES caverns. Research demonstrated that steel lining can provide a good airtightness under a high gas pressure [25]. Application of steel lining could not only extend the usable-ness of abandoned coal mines, but also liberate excessive production capacity, reducing the difficulty in reforming steel industry of China.

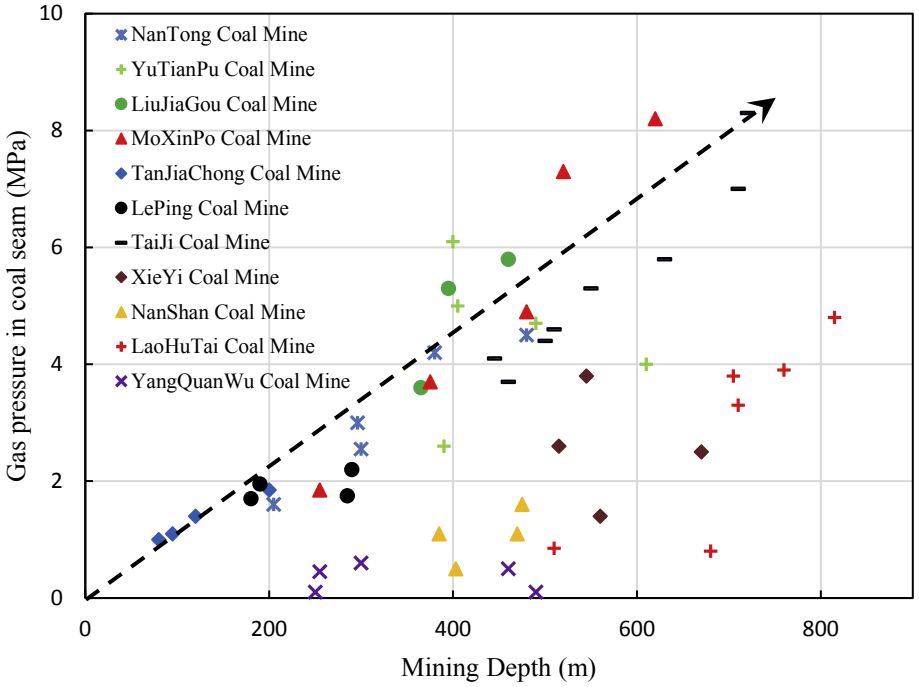

Fig. 21. Gas pressure *vs* mining depth in some typical mines (Data from Ref. [39]).

7. Conclusions

To utilize the intermittent wind and solar powers in the area where both are highly abundant, a hybrid wind-solar CAES system using an abandoned coal mine is proposed, in which the wind power drives compressors and the solar power heats the released air before expansion. Since water as a popular cooling media is frozen in Three North Region in China, PBTES is adopted because of its properties of low cost and high reliability. The system thermodynamic analysis and service potential for coal mine roadways is conducted. The obtained main results are as following:

(1) Exergy analysis shows that the maximum exergy loss is caused by throttling. In terms of underground space utilization, the outlet pressure of throttling valve is best at 4 MPa with the energy storage density being 2.99 kW h/m^3, when the maximum operational pressure is fixed at 7.5 MPa. The exergy loss of turbines takes up 5.51% of the total exergy. The remaining heats can be utilized by ORC system and thereby raise the system efficiency by 0.8%.

(2) Under the design conditions, the WE and SE are 64% and 25%, respectively. To ensure the temperature difference between outlet air of turbines and PBTES, the maximum solar heat storage rate is suggested at 0.855. The average system efficiency, power and EPV of an exemplary WS-CAES plant in Xinjiang Province with the storage capacity of 24,762 m^3 can reach 50.31%, 8.76 MW and 3.23 kW h/m^3, respectively.

(3) The system efficiency is independent of the ambient temperature. The output power and energy storage density rise a little with the increasing ambient temperature. The maximum acceptable permeability of concrete lining is calculated at 4.17×10^{-18} m^2. According to the analysis, the CAES cavern structure stability should rely on the concrete lining, while air tightness atmosphere should be given by the surrounding rock system.

(4) The surrounding rocks of main ventilation/haulage roadway below 600 m are able to have considerable air tightness, thus having a good potential to serve as compressed air storages. The air leakage rate of a mudstone with a permeability of 8.57×10^{-20} m^2 in one cycle is only 0.023%. Consequently, the average system efficiency reaches 50.29%.

Acknowledgments

This work was supported by the National Key R&D Program of China (2017YFC0804202), the Natural Science Fund (No. 41672292, 51604044), which are all greatly appreciated.

References

[1] Mittal S, Dai H, Fujimori S, Masui T. Bridging greenhouse gas emissions and renewable energy deployment target: comparative assessment of China and India. Appl Energy 2016;166:301–13.
[2] Squalli J. Renewable energy, coal as a baseload power source, and greenhouse gas emissions: evidence from U.S. state-level data. Energy 2017;127:479–88.
[3] Radgen P. Greenhous gas emissions reduction by motor systems—the case of compressed air systems in power generation and industry, Greenhouse Gas Control Technologies 7. Oxford: Elsevier Science Ltd; 2005. p. 1421–6.
[4] Bouman EA, Øberg MM, Hertwich EG. Environmental impacts of balancing offshore wind power with compressed air energy storage (CAES). Energy 2016;95(Supplement C):91–8.
[5] Liu J-L, Wang J-H. A comparative research of two adiabatic compressed air energy storage systems. Energy Convers Manag 2016;108:566–78.
[6] Lund H, Salgi G. The role of compressed air energy storage (CAES) in future sustainable energy systems. Energy Convers Manag 2009;50(5):1172–9.
[7] Chen L-X, Hu P, Sheng C-C, Xie M-N. A novel compressed air energy storage (CAES) system combined with pre-cooler and using low grade waste heat as heat source. Energy 2017;131(Supplement C):259–66.
[8] Kim MJ, Kim TS. Feasibility study on the influence of steam injection in the compressed air energy storage system. Energy 2017;141(Supplement C): 239–49.
[9] Tola V, Meloni V, Spadaccini F, Cau G. Performance assessment of Adiabatic Compressed Air Energy Storage (A-CAES) power plants integrated with packed-bed thermocline storage systems. Energy Convers Manag 2017;151(Supplement C):343–56.
[10] J. yuqiong, 2014. http://news.bjx.com.cn/html/20141024/557444.shtml.
[11] Fan J, Chen J, Jiang D, Ren S, Wu J. Fatigue properties of rock salt subjected to interval cyclic pressure. Int J Fatig 2016;90:109–15.
[12] Jiang D, Fan J, Chen J, Li L, Cui Y. A mechanism of fatigue in salt under discontinuous cycle loading. Int J Rock Mech Min Sci 2016;86:255–60.
[13] Fan J, Chen J, Jiang D, Chemenda A, Chen J, Ambre J. Discontinuous cyclic

loading tests of salt with acoustic emission monitoring. Int J Fatig 2017;94(1):140–4.
[14] Kapila S, Oni AO, Kumar A. The development of techno-economic models for large-scale energy storage systems. Energy 2017;140(Part 1):656–72.
[15] Kim YM, Shin DG, Favrat D. Operating characteristics of constant-pressure compressed air energy storage (CAES) system combined with pumped hydro storage based on energy and exergy analysis. Energy 2011;36(10):6220–33.
[16] Jabari F, Nojavan S, Mohammadi Ivatloo B. Designing and optimizing a novel advanced adiabatic compressed air energy storage and air source heat pump based μ-Combined Cooling, heating and power system. Energy 2016;116(Part 1):64–77.
[17] Kougias I, Szabó S. Pumped hydroelectric storage utilization assessment: forerunner of renewable energy integration or Trojan horse? Energy 2017;140(Part 1):318–29.
[18] Melikoglu M. Pumped hydroelectric energy storage: analysing global development and assessing potential applications in Turkey based on Vision 2023 hydroelectricity wind and solar energy targets. Renew Sustain Energy Rev 2017;72:146–53.
[19] Jannelli E, Minutillo M, Lubrano Lavadera A, Falcucci G. A small-scale CAES (compressed air energy storage) system for stand-alone renewable energy power plant for a radio base station: a sizing-design methodology. Energy 2014;78(Supplement C):313–22.
[20] Jubeh NM, Najjar YSH. Power augmentation with CAES (compressed air energy storage) by air injection or supercharging makes environment greener. Energy 2012;38(1):228–35.
[21] Szablowski L, Krawczyk P, Badyda K, Karellas S, Kakaras E, Bujalski W. Energy and exergy analysis of adiabatic compressed air energy storage system. Energy 2017;138(Supplement C):12–8.
[22] 2014. http://finance.sina.com.cn/chanjing/cyxw/20140117/085617987510.shtml.
[23] Kim H-M, Rutqvist J, Ryu D-W, Choi B-H, Sunwoo C, Song W-K. Exploring the concept of compressed air energy storage (CAES) in lined rock caverns at shallow depth: a modeling study of air tightness and energy balance. Appl Energy 2012;92:653–67.
[24] Rutqvist J, Kim H-M, Ryu D-W, Synn J-H, Song W-K. Modeling of coupled thermodynamic and geomechanical performance of underground compressed air energy storage in lined rock caverns. Int J Rock Mech Min Sci 2012;52:71–81.
[25] Rutqvist J, Ijiri Y, Yamamoto H. Implementation of the Barcelona Basic Model into TOUGH–FLAC for simulations of the geomechanical behavior of unsaturated soils. Comput Geosci 2011;37(6):751–62.
[26] Tian H, Du L, Wei X, Deng S, Wang W, Ding J. Enhanced thermal conductivity of ternary carbonate salt phase change material with Mg particles for solar thermal energy storage. Appl Energy 2017;204:525–30.
[27] Pelay U, Luo L, Fan Y, Stitou D, Rood M. Thermal energy storage systems for concentrated solar power plants. Renew Sustain Energy Rev 2017;79:82–100.
[28] Peng H, Yang Y, Li R, Ling X. Thermodynamic analysis of an improved adiabatic compressed air energy storage system. Appl Energy 2016;183:1361–73.
[29] Ortega-Fernández I, Zavattoni SA, Rodríguez-Aseguinolaza J, D'Aguanno B, Barbato MC. Analysis of an integrated packed bed thermal energy storage system for heat recovery in compressed air energy storage technology. Appl Energy 2017;205:280–93.
[30] Sciacovelli A, Li Y, Chen H, Wu Y, Wang J, Garvey S, Ding Y. Dynamic simulation of Adiabatic Compressed Air Energy Storage (A-CAES) plant with integrated thermal storage – link between components performance and plant performance. Appl Energy 2017;185(Part 1):16–28.
[31] Ji W, Zhou Y, Sun Y, Zhang W, An B, Wang J. Thermodynamic analysis of a novel hybrid wind-solar-compressed air energy storage system. Energy Convers Manag 2017;142:176–87.
[32] Guo H, Xu Y, Chen H, Zhou X. Thermodynamic characteristics of a novel supercritical compressed air energy storage system. Energy Convers Manag 2016;115:167–77.
[33] Tola V, Meloni V, Spadaccini F, Cau G. Performance assessment of Adiabatic Compressed Air Energy Storage (A-CAES) power plants integrated with packed-bed thermocline storage systems. Energy Convers Manag 2017;151:343–56.
[34] Hoseini M, Bindiganavile V, Banthia N. The effect of mechanical stress on permeability of concrete: a review. Cement Concr Compos 2009;31(4):213–20.
[35] Kameche ZA, Ghomari F, Choinska M, Khelidj A. Assessment of liquid water and gas permeabilities of partially saturated ordinary concrete. Construct Build Mater 2014;65:551–65.
[36] Li X, Xu Q, Chen S. An experimental and numerical study on water permeability of concrete. Construct Build Mater 2016;105:503–10.
[37] Abid M, Hou X, Zheng W, Hussain RR. High temperature and residual properties of reactive powder concrete – a review. Construct Build Mater 2017;147:339–51.
[38] Mostofinejad D, Nikoo MR, Hosseini SA. Determination of optimized mix design and curing conditions of reactive powder concrete (RPC). Construct Build Mater 2016;123:754–67.
[39] Yuan L. Coal seam gas content method is used to predict coal and gas outburst theory and technology. Science Press; 2014.
[40] Kelsall PC, Case JB, Chabannes CR. Evaluation of excavation-induced changes in rock permeability. Int J Rock Mech Min Sci Geomech Abstr 1984;21(3):123–35.
[41] Wang JA, Park HD. Fluid permeability of sedimentary rocks in a complete stress–strain process. Eng Geol 2002;63(3–4):291–300.
[42] Somerton WH, Söylemezoğlu IM, Dudley RC. Effect of stress on permeability of coal. Int J Rock Mech Min Sci Geomech Abstr 1975;12(5–6):129–45.
[43] Q.p.d.a.r. commission, 2017. http://www.360doc.com/content/17/0623/08/39179077_665.716110.shtml.
[44] 2017. http://www.china-nengyuan.com/news/6479.html.
[45] 2016. http://www.ocn.com.cn/chanjing/201606/kiotx27092950.shtml.
[46] W. Dingxiaolu, 2016. http://solar.ofweek.com/2016-05/ART-260009-8420-29093317.html.
[47] Zhang N, Lu X, McElroy MB, Nielsen CP, Chen X, Deng Y, Kang C. Reducing curtailment of wind electricity in China by employing electric boilers for heat and pumped hydro for energy storage. Appl Energy 2016;184:987–94.
[48] Bo W, Jingming L, Yi Z, Hongyan W, Honglin L, Guizhong L, Jingzhang M. Geological characteristics of low rank coalbed methane, China. Petrol Explor Dev 2009;36(1):30–4.
[49] Production of coalbed methane, 2017. http://www.bosidata.com/nengyuanshuju1703/831984NX6E.html.